MEMS Bragg grating force sensor

Reck, Kasper; Thomsen, Erik Vilain; Hansen, Ole

Published in:
Optics Express

Link to article, DOI:
10.1364/OE.19.019190

Publication date:
2011

Document Version
Publisher's PDF, also known as Version of record

MEMS Bragg grating force sensor

Kasper Reck,[1,*] **Erik V. Thomsen,**[1] **and Ole Hansen**[2]

[1]*Department of Micro- and Nanotechnology, Technical University of Denmark, DTU Nanotech, Building 345 East DK-2800 Kongens Lyngby, Denmark*

[2]*Also with Center for Individual Nanoparticle Functionality, CINF, Technical University of Denmark*

[*]*kasper.reck@nanotech.dtu.dk*

Abstract: We present modeling, design, fabrication and characterization of a new type of all-optical frequency modulated MEMS force sensor based on a mechanically amplified double clamped waveguide beam structure with integrated Bragg grating. The sensor is ideally suited for force measurements in harsh environments and for remote and distributed sensing and has a measured sensitivity of -14 nm/N, which is several times higher than what is obtained in conventional fiber Bragg grating force sensors.

OCIS codes: (130.3120) Integrated optics devices; (220.4880) Optomechanics; (230.1150) All-optical devices.

References and links

1. Z. Zhou and J. Ou, "Techniques of temperature compensation for FBG strain sensors used in long-term structural monitoring," Proc. SPIE, 167–172 (2005).
2. H. Fu, J. Fu, and X. Qiao, "High sensitivity fiber Bragg grating pressure difference sensor," Chin. Opt. Lett. **2,** 621–623 (2004).
3. J. A. Plaza, A. Llobera, C. Dominguez, J. Esteve, I. Salinas, J. Garcia and J. Berganzo, "BESOI-based integrated optical silicon accelerator," J. Microelectromech. Syst. **13,** 355–364 (2004).
4. D. Yin, D. W. Deamer, H. Schmidt, J. P. Barber, and A. R. Hawkins, "Integrated optical waveguides with liquid cores," Appl. Phys. Lett. **85,** 3477–3479 (2004).
5. X.-jin Lia, C.-jun Qiu, Y.-long Deng, W. Qu, and J.-N. He, "An MEMS optical fiber pressure sensor based on a square silicon diaphragm: numerical simulation and experimental verification," Int. J. Nonlinear Sci. Numer. Simul. **11,** 225–229 (2010).
6. Q. Wang, Z. Fen, F. Deng, G. Huang, L. Yan, and Y. Dai, "Fiber Bragg gratings for strain sensing in high temperature superconducting magnet," IEEE Trans. Appl. Supercond. **17,** 2377–2380 (2007).
7. Y. I. Rzhavin, "Fiber-optic polarization pressure sensor," Meas. Tech. **45,** 738–741 (2002).
8. E. Bonnotte, C. Gorecki, H. Toshiyoshi, H. Kawakatsu, H. Fujita, K. Worhoff and K. Hashimoto, "Guided-wave acoustooptic interaction with phase modulation in a ZnO thin-film transducer on an Si-based integrated Mach-Zehnder interferometer," J. Lightwave Technol. **17,** 35–42 (1999).
9. D. Graham-Rowe, "Sensors take the strain," Nat. Photonics **1,** 307–309 (2007).
10. W. Zhang, E. Li, J. Xi, J. Chicharo and X. Dong, "Novel temperature-independent FBG-type force sensor," Meas. Sci. Technol. **16,** 1600–1604 (2005).
11. L. Ren, J. Chen, H.-N. Li, G. Song and X. Ji, "Design and application of a fiber Bragg grating strain sensor with enhanced sensitivity in the small-scale dam model," Smart Mater. Struct. **18,** 035015 (2009)
12. W. Zhang, X. Dong, Q. Zhao, G. Kai and S. Yuan, "FBG-type sensor for simultaneous measurement of force (or displacement) and temperature based on bilateral cantilever beam," IEEE Photon. Technol. Lett. **13,** 1340–1342 (2001).
13. L. Eldada, "Polymer integrated optics: promise vs. practicality," Org. Photon. Mater. Dev. IV **4642,** 11–22 (2002).

1. Introduction

All-optical sensors are well suited for a wide range of different applications, e.g. structural strain sensing [1], pressure sensing [2], acceleration [3] and biochemical sensing [4]. While

#150617 - $15.00 USD Received 8 Jul 2011; revised 24 Aug 2011; accepted 24 Aug 2011; published 19 Sep 2011

all-optical sensors can be amplitude [5], frequency [6], polarization [7] or phase modulated [8] the all-optical sensor types most often encountered in literature within strain, pressure and force sensing are the amplitude and frequency modulated sensors. Amplitude modulated sensors usually have a very high sensitivity at the cost of increased transmission noise sensitivity and maximum one sensor per communication line. Frequency modulated sensors typically have lower sensitivity than amplitude modulated sensors and they rely on an absolute frequency shift, however, frequency modulated sensors are almost immune to amplitude affecting noise sources and can easily be integrated in large distributed systems by wavelength division multiplexing. One of the most successful all-optical frequency modulated sensor today is the fiber Bragg grating (FBG) sensor [9]. The typical cross-sectional dimensions of the sensing element in FBGs is in the order of 100-200 μm (125 μm for a standard optical fiber). These relatively large physical dimensions combined with limitations with respect to material choice and refractive index modulation gives FBGs an inherently low sensitivity. However, using MEMS technology and high refractive index contrast materials, the cross-sectional dimensions of the sensing element can be reduced by approximately one order of magnitude. Furthermore, proper mechanical design allows for integrated amplification of the force induced strain which is not easily obtainable in FBGs.

2. Theory

The basic sensing principle of FBGs as well as MEMS Bragg grating (MBG) sensors is modulation of the Bragg wavelength λ_B by e.g. strain; the Bragg wavelength is obtained from

$$\lambda_B = 2n_{\text{avg}}\Lambda,$$

where n_{avg} is the geometrically averaged effective index and Λ is the period of the Bragg grating. The sensitivity or relative Bragg wavelength shift is given by

$$\frac{\Delta\lambda_B}{\lambda_B} = (\alpha+\zeta)\Delta T + (1-p_e)\varepsilon_\ell,$$

where α is the thermal expansion coefficient of the part of the waveguide containing the grating, ζ is the thermooptic coefficient, p_e is the photoelastic coefficient for longitudinal strain and ε_ℓ is the longitudinal strain. In the following analysis we shall neglect the thermooptic effect, since it can be separated by a differential measurement, and the photoelastic effect since it reduces to a factor of proportionality to the strain sensing term.

In FBG force sensors, the force is applied longitudinal or transversal, and in both cases the longitudinal strain is measured. In the case of a longitudinal force load the force sensitivity, however, is rather low due to the high stiffness of the structure; the force sensitivity may, however, be improved using mechanical strain amplification.

We consider a structure, shown schematically in Fig. 1, built from two prismatic beam (each of length L, width W and thickness H) joined together at an angle of $\pi - 2\theta$ by a rigid center boss, while the other ends are assumed rigidly clamped. The force load is applied to the center boss joining the two beams. The load force F is balanced by shear V and normal N forces in the beams, such that a static vertical force balance requires

$$F = 2V\cos\theta - 2N\sin\theta, \tag{1}$$

where V and N are the force magnitudes in the left hand beam. In the extreme case of $\theta = 0$ the normal force vanish (in a first approximation) and the load is balanced entirely by the shear forces causing bending of the beams and essentially zero shift of the Bragg wavelength. In the other extreme case $\theta = \pi/2$ the shear force vanish and the load is balanced by normal forces in

#150617 - $15.00 USD Received 8 Jul 2011; revised 24 Aug 2011; accepted 24 Aug 2011; published 19 Sep 2011

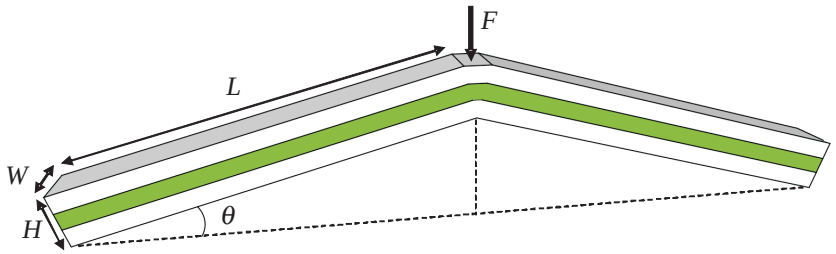

Fig. 1. Sketch of the structure used for strain amplification. The structure comprises two clamped beams joined together at an angle $\pi - 2\theta$ by a stiff center boss. A force F to be measured is applied to the center boss. At a specific angle, $0 < \theta < \pi/2$, the longitudinal strain in the Bragg grating (green) is maximized for a fixed force F.

the beams causing elongation or compression of the beams and a finite Bragg wavelength shift results. In general both shear and normal forces in the beams are finite causing both longitudinal and transversal displacements u and w, respectively, of the beams. The boss, however, can only displace in the vertical direction due to symmetry, and thus the beam displacements $u_L = u(L)$ and $w_L = w(L)$ at the boss are subject to the geometrical restriction

$$w_L \sin\theta = -u_L \cos\theta. \tag{2}$$

The longitudinal beam displacement is related to the normal force, which is considered constant throughout a beam, and thus

$$u_L = L\varepsilon_\ell = NL/(EWH), \tag{3}$$

where $\varepsilon_\ell = N/(EWH)$ is the longitudinal strain, and E is Young's modulus for the beam material. The transversal displacement may be found as the solution to Euler's beam equation

$$EIw'''' - Nw'' = q, \tag{4}$$

with the boundary conditions $w(0) = 0$, $w'(0) = w'(L) = 0$, and $w(L) = w_L$, due to clamping of the ends of the beams, and with the distributed load $q = 0$; here $I = WH^3/12$ is the area moment of inertia for the beam. In most practical cases the coupling to the normal force may be ignored when Euler's beam equation is solved and then the result is $w(x) = w_L x^2 (3L - 2x)/L^3$, while the full solution is given in the Appendix. The shear force and the beam deflection are related through $V = -EIw'''$, and thus $V = 12EIw_L/L^3 = EWH^3 w_L/L^3$. From the force balance, Eq. (1), the geometrical restriction Eq. (2) and Eq. (3) we may then solve for the normal force

$$N = -\frac{F\tan\theta}{2\left(\tan\theta\sin\theta + \left(\frac{H}{L}\right)^2\cos\theta\right)}, \tag{5}$$

and the longitudinal strain

$$\varepsilon_\ell = -\frac{F}{2EWH}\frac{\tan\theta}{\left(\tan\theta\sin\theta + \left(\frac{H}{L}\right)^2\cos\theta\right)}. \tag{6}$$

The longitudinal strain is seen to be maximized at the angle $\theta_{\max}$

$$\theta_{\max} = \arcsin\frac{H}{\sqrt{L^2 - H^2}} = \arctan\frac{H}{\sqrt{L^2 - 2H^2}} \simeq \frac{H}{L}, \tag{7}$$

#150617 - $15.00 USD Received 8 Jul 2011; revised 24 Aug 2011; accepted 24 Aug 2011; published 19 Sep 2011

where the approximation is valid for $H/L \ll 1$. At this angle the longitudinal strain becomes

$$\varepsilon_{\ell_{\max}} = -\frac{F}{2EWH}\frac{L}{2H\sqrt{1-\left(\frac{H}{L}\right)^2}} \simeq -\frac{FL}{4EWH^2}, \tag{8}$$

where the approximation is valid for $H/L \ll 1$. It follows that the longitudinal strain at $\theta_{\max}$ is amplified a factor $\sim L/(2H)$ compared to the longitudinal strain at $\theta = \pi/2$.

Due to the stiffness of the joining boss changes in the joining angle under load is a second order effect, and as a result the longitudinal strain increases linearly with the load force.

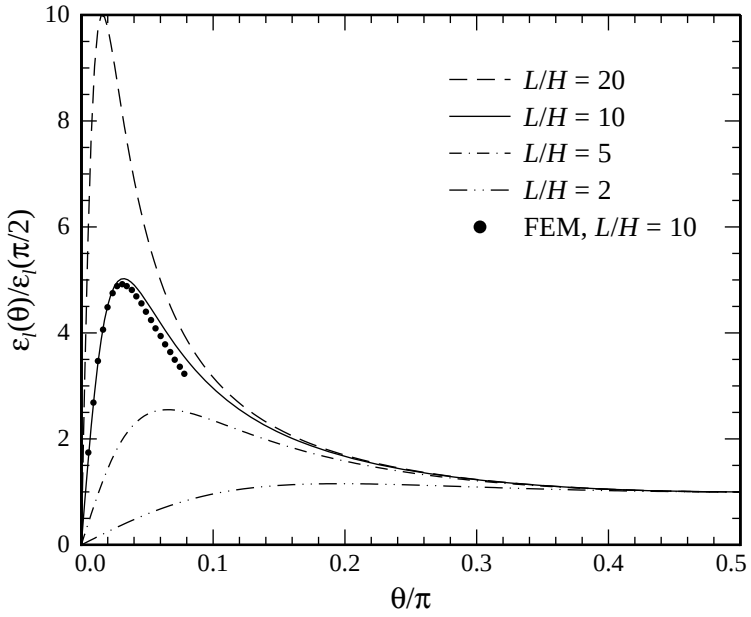

Fig. 2. Normalized longitudinal strain $\varepsilon_\ell(\theta)/\varepsilon_\ell(\pi/2)$ as function of beam angle θ shown for four different aspect ratios L/H. As the aspect ratio of the beam increases, the strain is increased and the peak of maximum strain shifts towards lower angles. For the aspect ratio $L/H = 10$ results from a FEM calculation are also shown (• symbol); the FEM results are seen to agree well with the analytical calculation.

The longitudinal strain, Eq. (6), normalized with respect to the strain at $\theta = \pi/2$ (i.e. a longitudinal loaded FBG) as function of beam angle θ is plotted in Fig. 2 for different aspect ratios L/H. As expected the normalized longitudinal strain is zero for $\theta = 0$ and has a maximum at an angle close to zero. When the aspect ratio is increased, the relative strain increases and the angle of maximum strain is reduced. In Fig. 2 results from a Finite Element Model (FEM) calculation ($L = 150$ μm, $W = 15$ μm, $H = 15$ μm) are also shown. The normalized strain calculated using FEM is seen to agree very well with the analytical calculation; in particular, the peak in relative strain at a low angle is well reproduced.

For materials such as silicon and silicon dioxide, aspect ratios in excess of 1:10 are routinely fabricated using MEMS technology. A significant sensitivity increase compared to FBGs is thus obtainable using MEMS technology, in particular when also a reduction of the cross-sectional dimensions by an order of magnitude is taken into account.

#150617 - $15.00 USD Received 8 Jul 2011; revised 24 Aug 2011; accepted 24 Aug 2011; published 19 Sep 2011

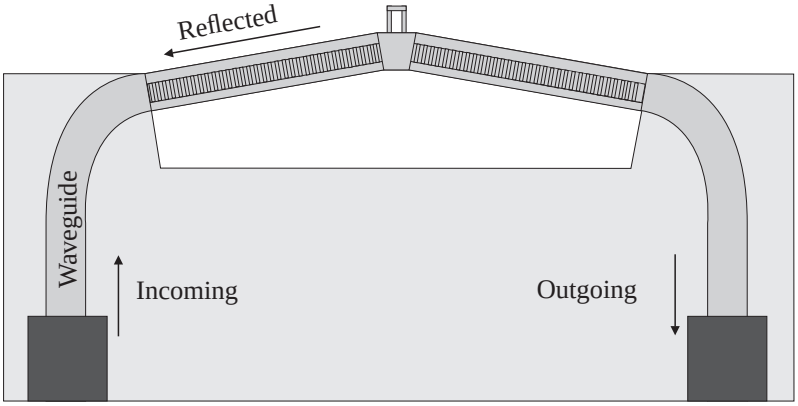

Fig. 3. The MBG sensor consists of a u-shaped waveguide connecting the fiber connect grooves at the bottom to the double beam sensing element at the top.

A note of caution, the structure is also sensitive to out of the plane bending of the beams. To ensure proper operation of the sensor it is important that the load force is applied such that out of the plane bending is avoided; this is particularly important when the beam is under compressive load.

3. Design and fabrication

A sketch of the fabricated MBG sensor is shown in Fig. 3. Light is coupled into the chip from an optical fiber using one of the two fiber connect grooves located at the lower boundary of the sensor chip. Silicon oxynitride (SiON) optical waveguides run from the fiber connect grooves to the double beam structure with integrated Bragg gratings located at the upper half of the chip. The radius of curvature of the waveguide is large enough to minimize bending losses.

The sensor is fabricated from a 350 μm thick silicon wafer and the chip measures 6×5 mm^2. The process flow for fabrication of the sensor is shown in Fig. 4. The sensor is fabricated from an atmospheric pressure oxidized (APOX) silicon wafer with 8.2 μm thermal SiO_2 (a). The oxide will serve as the lower waveguide cladding layer. The waveguide core is made from a 2.4 μm thick SiON grown using plasma enhanced chemical vapor deposition (PECVD) (b). The Bragg grating structure is defined in the positive resist ZEP520a using e-beam lithography (EBL). By e-beam evaporation of 70 nm aluminum, the grating is transferred to an aluminum mask in a lift-off process. The grating is then etched in the waveguide core using advanced oxide etching (AOE) for a total corrugation depth of 1 μm (c). Borophosphosilicate glass (BPSG) with a thickness of 4.8 μm is deposited using PECVD and annealed at 1000 °C for 6 hours (d). This BPSG layer serves as the upper cladding layer and will reflow during annealing to improve the poor as deposited step coverage of the PECVD process. A membrane is created from the backside using UV lithography (UVL) followed by AOE and deep reactive ion etch (DRIE). The etch stops at the lower cladding layer due to the high etch selectivity of silicon over silicon dioxide (e). Likewise, the fiber grooves are fabricated using UVL followed by AOE and DRIE (f). The final step is to define and release the waveguides, which is done by UVL and AOE (g).

The final device after dicing is shown in Fig. 5; both a micrograph of the full 6×5 mm^2 chip (Fig. 5a) as well as a close-up image of the sensor beam region (Fig. 5b) are shown. The fabricated MBG test chip has the sensor beam dimensions $L = 150$ μm, $W = 30$ μm, and $H = 15.4$ μm and a geometrically averaged Young's modulus of 133 GPa for the sensor beams.

#150617 - $15.00 USD Received 8 Jul 2011; revised 24 Aug 2011; accepted 24 Aug 2011; published 19 Sep 2011

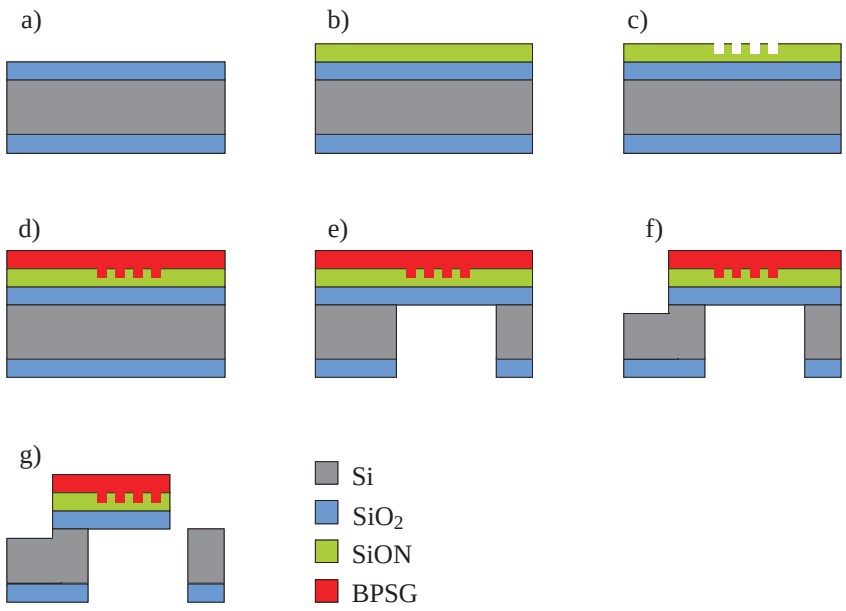

Fig. 4. Process flow for the sensor. Starting with an APOX wafer (a), 2.4 μm SiON is deposited using PECVD (b) in which a waveguide core and Bragg grating is written using EBL and AOE (c). A 4.8 μm thick layer of BPSG is deposited using PECVD (d) and a membrane is etched from the backside using AOE and DRIE (e). Finally the fiber grooves are made using AOE and DRIE (f) and the double beam is then released from from the membrane in an AOE etch which also defines the waveguide cladding (g).

4. Results

For characterization of the sensor a Koehras SuperK supercontinuum laser emitting in the visible range was connected to the input of the test chip through a fiber optic circulator and a SMF-28 optical fiber; the reflected signal was measured using an Agilent AQ-6315A optical spectrum analyzer. A load force was applied to the beam using a micro needle attached to a force sensor (Strain Measurement Devices s415 button cell) mounted on a micrometer stage. The measured reflection spectra at three different applied load forces are shown in Fig. 6a where a clear shift of the reflection spectra due to the load force is seen. To extract the experimental Bragg wavelength (interpreted as the center wavelength of the reflection peak) Gaussian functions were fitted to the measured spectra, from the fits the full width at half maximum is found to 2.3 nm, which is larger than what is generally found in FBGs due to the higher index modulation in the MBG. The experimental Bragg wavelength for the unloaded beam is $\lambda_B = 787.4$ nm. The extracted shift in Bragg wavelength as function of applied force is shown in Fig. 6b, where the sensitivity is seen to be -14 nm/N as extracted from the slope of linear fit to the experimental data. This should be compared to the sensitivities of typical FBG sensors found in literature, e.g. 0.1 pm/N [10], 2.2 nm/N [11] and 1.046 nm/N [12], while also noting that the MBG offers a much smaller and mechanical robust design with an inherent mass production potential.

Temperature measurements were conducted using a 82 W Peltier element for heating the sensor and a K-type thermocouple for measuring the temperature change. The unloaded Bragg wavelength shift as a function of a temperature shift is shown in Fig. 7, where the temperature of

#150617 - $15.00 USD Received 8 Jul 2011; revised 24 Aug 2011; accepted 24 Aug 2011; published 19 Sep 2011

(a) (b)

Fig. 5. a) The finished chip with the waveguide (u-shaped) extending from the two fiber grooves at the bottom of the chip to the double beam at the top of the chip. b) The final double beam waveguide structure after dicing. A small amount of residues from the carrier membrane are seen around the double beam. With a thickness of < 50 nm such residues have almost no effect on the beam deflection.

the chip was increased from 23.9°C to approximately 40°C and the reflection spectra recorded at six discrete temperatures. From the measured Bragg wavelengths a temperature sensitivity of approximately 30 pm/K results. The high temperature sensitivity is primarily due to a large thermooptic coefficient of the waveguide material [13]. With this high temperature sensitivity a differential measurement strategy, where both a loaded and an unloaded sensor on the same chip are measured simultaneously to eliminate the thermal signal, is advantageous.

Power loss measurements on straight waveguides without Bragg gratings show a coupling loss of approximately 6 dB per coupling, while the transmission loss is less than 1 dB. The coupling losses are approximately 2 dB larger than expected from mode overlap integral calculations, indicating a slight misalignment between the optical fiber and the waveguide. In order to reduce the coupling losses further, tapering of either the optical fiber or the waveguide could be applied.

5. Conclusion

We have presented a new all-optical frequency modulated MEMS force sensor based on mechanically amplified deformation of an integrated nanoscale Bragg grating. From analytical model calculations an optimal sensor design has been developed and a sensor fabricated. Measurements of the wavelength shift as function of applied force have been conducted resulting in an experimental sensitivity of -14 nm/N, in agreement with the developed analytical model. This sensitivity is much higher than what is found using conventional FBG strain sensors. Temperature measurements show a temperature sensitivity of approximately 30 pm/K, which is attributed primarily to thermooptic effects. Coupling and propagation losses have been measured to 6 dB and less than 1 dB, respectively. The high sensitivity is obtained at the cost of a significant sensitivity to out of the plane bending, and a rather fragile structure.

#150617 - $15.00 USD Received 8 Jul 2011; revised 24 Aug 2011; accepted 24 Aug 2011; published 19 Sep 2011

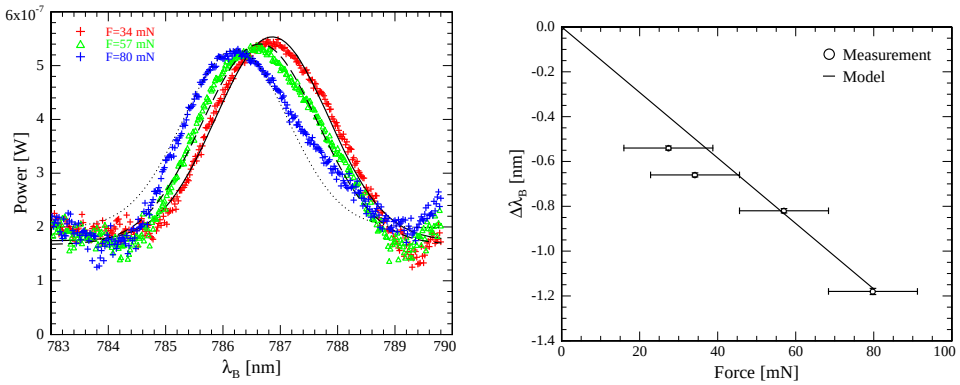

(a) (b)

Fig. 6. (a) The measured reflection spectra at three different loads. The average full width half maximum is 2.3 nm. (b) The measured change in Bragg wavelength as function of applied force. The measured Bragg wavelength shifts are seen to be in good agreement with the model calculations. The sensitivity is found to -14 nm/N.

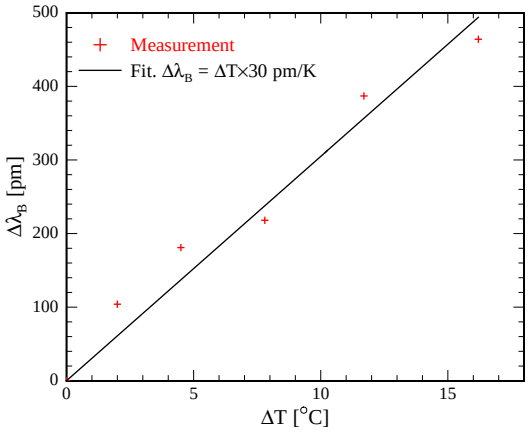

Fig. 7. The change in Bragg wavelength due to temperature starting from 23.9°C. From the linear fit the temperature sensitivity is found to 30 pm/°C.

Appendix

The exact solution to Euler's equation, Eq. (4), including the normal force coupling is

$$w(x) = w_L \frac{(\varkappa x - \sin \varkappa x)\sin \varkappa L + (1-\cos \varkappa L)(\cos \varkappa x - 1)}{2(\cos \varkappa L - 1) + \varkappa L \sin \varkappa L} \tag{9}$$

$$\simeq w_L x^2 (3L-2x)/L^3 + \mathscr{O}(\varkappa^2) \tag{10}$$

where the parameter $\varkappa$ is obtained from $\varkappa^2 = -N/(EI)$. The exact solution is needed in case a static pre-strain is used, since in such cases $\varkappa L \ll 1$ may not be fulfilled.

#150617 - $15.00 USD Received 8 Jul 2011; revised 24 Aug 2011; accepted 24 Aug 2011; published 19 Sep 2011

Acknowledgments

Center for Individual Nanoparticle Functionality (CINF) is sponsored by The Danish National Research Foundation.

#150617 - $15.00 USD Received 8 Jul 2011; revised 24 Aug 2011; accepted 24 Aug 2011; published 19 Sep 2011